

Comparative Study of Magnetocaloric Properties for Gd³⁺ Compounds with Different Frustrated Lattice Geometries

EliseAnne C. Koskelo^{1,*†}, Paromita Mukherjee,¹ Cheng Liu,¹ Alice C. Sackville Hamilton,¹ Harapan S. Ong,¹ Claudio Castelnovo,¹ M.E. Zhitomirsky,² and Siân E. Dutton^{1,†}

¹*Department of Physics, University of Cambridge, Cambridge, CB3 0HE, United Kingdom*

²*Université Grenoble Alpes, CEA, IRIG, PHELIQS, 38000 Grenoble, France*



(Received 3 March 2023; revised 26 June 2023; accepted 10 July 2023; published 31 July 2023)

As materials with suppressed ordering temperatures and enhanced ground-state entropies, frustrated magnetic oxides are ideal candidates for cryogenic magnetocaloric refrigeration. While previous material design focused on tuning the magnetic moments, their interactions, and the density of moments on the lattice, relatively little attention has been paid to frustrated lattices. Prior theoretical work has shown that the magnetocaloric cooling rate at the saturation field is proportional to a macroscopic number of soft mode excitations that arise due to the classical ground-state degeneracy. The number of these modes is directly determined by the geometry of the frustrated lattice. For corner-sharing geometries, the pyrochlore lattice has 50% more modes than the garnet and kagome lattices, whereas the edge-sharing fcc lattice has only a subextensive number of soft modes. Here we study the role of soft modes in the magnetocaloric effect of four large-spin Gd³⁺ ($L = 0, J = S = 7/2$) Heisenberg antiferromagnets on a kagome, garnet, pyrochlore, and fcc lattice down to $T = 2$ K. By comparing measurements of the magnetic entropy change ΔS_m of these materials at fields up to 9 T with predictions obtained with use of mean-field theory and Monte Carlo simulations, we are able to understand the relative importance of spin correlations and quantization effects. We observe that tuning the value of the nearest-neighbor coupling has a more significant contribution to the magnetocaloric entropy change in the liquid-He cooling regime (2–20 K) than tuning the number of soft mode excitations. Our results provide a base for future refrigerant-material design in terms of dimensionality, degree of magnetic frustration, and lattice geometry.

DOI: 10.1103/PRXEnergy.2.033005

I. INTRODUCTION

The ever-increasing need for refrigeration in modern technologies, as well as the scarcity of helium, has motivated the search for sustainable cooling alternatives [1]. One such alternative cooling technique is adiabatic demagnetization refrigeration (ADR) based on the magnetocaloric effect. Historically, ADR was the first cooling method able to reach temperatures below 1 K [2]. Today, ADR coolers are widely used on satellites under microgravity conditions to increase the sensitivity of

telescope detectors. ADR technology is also attractive for laboratory applications since it enables fast low-temperature characterization of quantum materials and nanodevices. The expanding niche for low-temperature ADR applications requires a systematic study of the magnetocaloric effect across a wide range of magnetic materials with the aim of optimizing performance and finding the most suitable refrigerant for a given range of temperatures and fields.

Common early adiabatic demagnetization refrigerants were based on dilute paramagnetic salts such as cerous magnesium nitrate (CMN) and ferric ammonium (FAA) [3]. Research interests shifted later from dilute paramagnetic salts and superparamagnets to dense magnetic lattice magnets, when it was shown that frustration can enable an enhanced magnetocaloric effect via (i) a suppressed ordering temperature at the same magnetic density and (ii) a large ground-state entropy [4]. Gd₃Ga₅O₁₂, perhaps the most-well-known frustrated magnetocaloric material, exhibits a magnetic entropy difference of 13.0 JK⁻¹ mol_{Gd}⁻¹ in a field change from 7 T to zero field at 2 K, with cooling capabilities down to approximately 0.8 K [5,6].

*eck34@cantab.ac.uk

†sed33@cam.ac.uk

[‡]Present address: Department of Physics, Harvard University, Cambridge, Massachusetts 02138, USA.

Published by the American Physical Society under the terms of the [Creative Commons Attribution 4.0 International license](#). Further distribution of this work must maintain attribution to the author(s) and the published article's title, journal citation, and DOI.

Other notable Gd^{3+} examples include the inorganic frameworks GdF_3 ($15.3 \text{ JK}^{-1} \text{ mol}_{\text{Gd}}^{-1}$) and Gd(OH)F_2 ($16.3 \text{ JK}^{-1} \text{ mol}_{\text{Gd}}^{-1}$), the dense metal-organic framework Gd(HCOO)_3 ($16.3 \text{ JK}^{-1} \text{ mol}_{\text{Gd}}^{-1}$), and the frustrated monazite antiferromagnet GdPO_4 ($15.6 \text{ JK}^{-1} \text{ mol}_{\text{Gd}}^{-1}$), all again in a field change from 7 T to zero field at 2 K [5,7–9].

In the case of Heisenberg Gd^{3+} , current magnetocaloric research for cooling in the liquid-He regime has focused on minimizing anisotropy of magnetic ions and their superexchange interactions to maximize spin polarizability [5,8,10]. However, using the subtle effects of magnetic frustration to enhance the magnetocaloric effect and to suppress the magnetic ordering temperature remains a relatively unexplored area of research [11,12]. In a system with strong magnetic frustration, the geometry of the magnetic lattice leads to a degeneracy in the magnetic ground state and a significant suppression of the magnetic ordering temperature. In frustrated magnetic oxides, the main tuning parameters are the magnetic ions and the atomic lattice. In this way, the superexchange and dipolar interactions and the crystal electric field environment of individual ions are manipulated.

In the case where dipolar and crystal electric field contributions are negligible, prior theoretical work has shown that the lattice geometry can dictate an enhancement of the magnetocaloric cooling rate, $(\partial T / \partial H)_{S_m} \propto -(\partial S_m / \partial H)_T$, that scales with the macroscopic number of soft modes N_4 at the saturation field [4]. The soft modes are ultimately a result of the macroscopic ground-state entropy that frustration introduces. These modes have been modeled for the three corner-sharing geometries shown in Fig. 1: the pyrochlore lattice, with the number of pyrochlore modes scaling as N , and the garnet and kagome lattices, with $2N/3$ soft modes, where N is the number of lattice sites [4]. Figure 1 also shows an edge-sharing geometry: the fcc lattice, for which the number of soft modes has not been reported.

In this work, we seek to test experimentally the role of these fundamental soft modes in the measured magnetocaloric effect in four representative frustrated oxide materials in the liquid-He regime (2–20 K). Of particular interest is answering the question of the optimal frustrating geometry to inform future magnetocaloric material design. Four Gd^{3+} -based oxides were chosen as model systems since the contribution of crystal electric field effects to the magnetism are negligible ($L = 0$ and hence $J = S = 7/2$ and $g_J = g = 2$). The four compounds investigated are $\text{Gd}_3\text{Mg}_2\text{Sb}_3\text{O}_{14}$, in which the Gd^{3+} ions lie on kagome layers separated by triangular layers of nonmagnetic Mg^{2+} ions [13]; $\text{Gd}_3\text{Ga}_5\text{O}_{12}$, in which Gd^{3+} ions lie on two interpenetrating rings of triangles [14]; $\text{Gd}_2\text{Sn}_2\text{O}_7$, in which the Gd^{3+} ions form a pyrochlore lattice (corner-sharing tetrahedra); and $\text{Ba}_2\text{GdSbO}_6$, an fcc lattice of Gd^{3+} ions (edge-sharing tetrahedra).

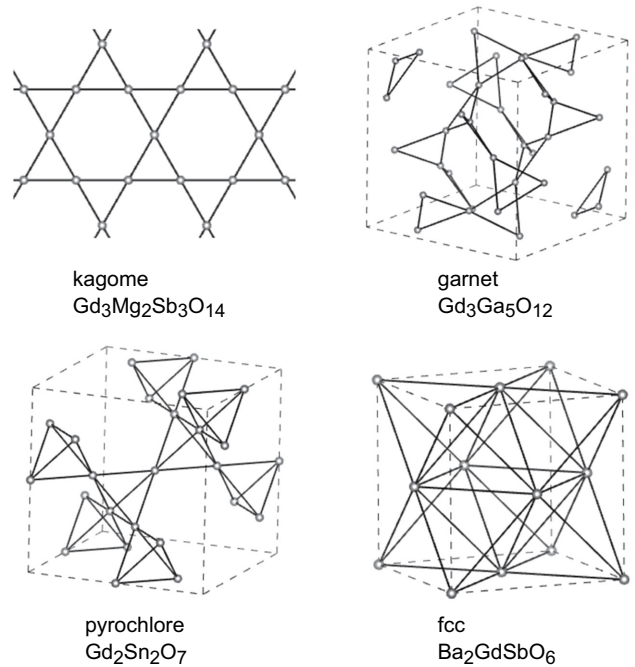


FIG. 1. Frustrated lattice geometries in two dimensions (kagome) and three dimensions (garnet, pyrochlore, and fcc).

We find that, upon normalization for the differences in superexchange across the materials, the normalized magnetic entropy change $\sqrt{J_1} \Delta S_m$ in this temperature range qualitatively scales with the number of soft modes for the 3D lattices as predicted in Ref. [4]. However, we find that the fcc lattice exhibits a 30%–95% greater magnetic entropy change ΔS_m than the corner-sharing lattices, which can be attributed to its paramagnetic response [15]. We compare the experimental results with Monte Carlo simulations of classical Heisenberg spins as well as with mean-field superexchange calculations in the paramagnetic regime that account for the quantized nature of the spins. These allow us to show that, in the temperature and field regimes of interest in this study, the effect of correlations is dominant over quantization in corner-sharing compounds, whereas the opposite is true for the fcc case. The fact that the magnetocaloric cooling rate of the corner-sharing geometries cannot be fully described by a mean-field superexchange model in the paramagnetic regime is consistent with a significant contribution of soft modes to the total magnetic entropy change measured.

For the compounds studied, we find that the paramagnetic contribution to the magnetic entropy outweighs that of geometric frustration. In particular, the threefold reduction in the superexchange J_1 of the garnet compound ($J_1 \sim 300 \text{ mK}$ [15]) results in a 50% increase in the magnetic entropy change extracted in comparison with the pyrochlore lattice. Our results allow us to demonstrate that combining a frustrated magnetic lattice and

a small exchange interaction results in an enhancement of the magnetocaloric effect for Heisenberg spins in the liquid-He regime. The future of magnetocaloric material design should make use of both these factors, allowing the possibility of significantly enhanced cooling at lower temperatures, where soft modes become the dominant contribution.

II. SOFT MODE MODEL: VALIDITY IN THE LIQUID-He REGIME

In prior work [4], one of us predicted a strongly enhanced magnetocaloric effect for geometrically frustrated magnets with high classical degeneracy in the ground state. The work also included classical Monte Carlo simulations, which are generally valid for large- S magnetic materials, for Heisenberg antiferromagnets with three typical frustrated geometries based on corner-sharing plaquettes: the 2D kagome lattice (a network of corner-sharing triangles), the garnet lattice (its 3D analogue), and the pyrochlore lattice (a network of corner-sharing tetrahedra); see Fig. 1. Here we revisit these geometries and compare them with an fcc lattice.

The spin Hamiltonian consists of a nearest-neighbor (NN) superexchange term, assumed to be uniform across all NN pairs, and a Zeeman term:

$$\hat{\mathcal{H}} = J_1 \sum_{\langle ij \rangle} \mathbf{S}_i \cdot \mathbf{S}_j - \mathbf{H} \cdot \sum_i \mathbf{S}_i, \quad (1)$$

where J_1 is the NN superexchange and a factor $g\mu_B$ has been absorbed into the definition of the field H for convenience. Dipolar interactions are also present in the system, but we disregard them in our simulations. Considering the system parameters reported Table II, we expect this to be a reasonable approximation for the three corner-sharing lattices. In the fcc system, superexchange and dipolar interactions at nearest-neighbor distance are of similar strength; however, they are small compared to temperatures in the range of interest in our study, and therefore truncating them to nearest-neighbor distance is a valid approximation.

In the low-temperature cooperative paramagnetic state, a condensation of a macroscopic number N_4 of soft modes [16] at the saturation field H_{sat} is predicted to occur, due to the enhanced ground-state entropy afforded by the underconstraint of frustration [4]. In contrast, ordered nonfrustrated antiferromagnets exhibit a canted phase for fields in the range $0 < H < H_{\text{sat}}$, and at $H = H_{\text{sat}}$ the magnon gap closes only at a single point $k = Q$ in momentum space, which becomes an ordering wave vector for the canted antiferromagnetic state for $H < H_{\text{sat}}$. Soft modes have been measured experimentally in $\text{Gd}_3\text{Ga}_5\text{O}_{12}$ and correspond to spin waves localized to ten site loops [17]. An example of the predicted magnon dispersion for the kagome lattice at H_{sat} is shown in Fig. 2, while dispersions for the pyrochlore and fcc lattices can be found

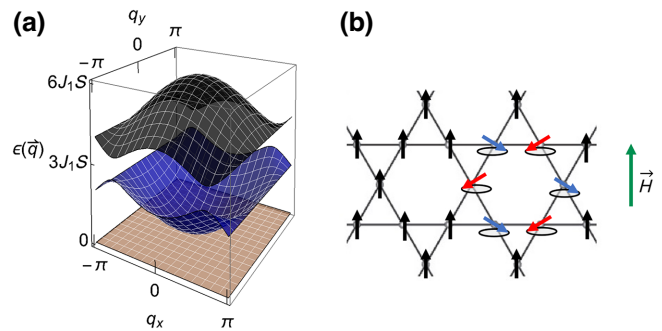


FIG. 2. (a) Predicted magnon dispersion of Heisenberg spins on the kagome lattice at $H_{\text{sat}} = 6J_1S$ [4]. The dispersionless soft modes are indicated by the flat brown surface at zero energy. (b) A possible spin arrangement in a kagome soft mode in which spins around a single hexagonal plaquette (red or blue) alternatively cant in directions perpendicular to the applied field.

in Refs. [4] and [18], respectively. The saturation field H_{sat} , defined as the threshold beyond which the energy becomes dominated by the Zeeman term, has been predicted [4] to be $6J_1S$ for the kagome and garnet lattices and $8J_1S$ for the pyrochlore lattice; see Table I. Using the same frustrated block decomposition [19], we obtain here $H_{\text{sat}} = 16J_1S$ for the nearest-neighbor fcc antiferromagnet (see Appendix A).

The magnetocaloric rate, $(\partial S_m / \partial H)_T$, at the saturation field is predicted to follow the scaling relation

$$\left(\frac{\partial S_m}{\partial H} \right)_{T, N_4} \propto -\frac{N_4}{\sqrt{J_1 T}} \quad \text{at } H = H_{\text{sat}}. \quad (2)$$

TABLE I. Predicted number of soft modes N_4 for a lattice with N sites of Heisenberg spins and predicted saturation field $H_{\text{sat, theory}}$ [4] versus measured saturation field $H_{\text{sat, obs}}$ for $\text{Gd}_3\text{Ga}_5\text{O}_{12}$, $\text{Gd}_3\text{Mg}_2\text{Sb}_3\text{O}_{14}$, $\text{Gd}_2\text{Sn}_2\text{O}_7$, and $\text{Ba}_2\text{GdSbO}_6$. The observed saturation field, $H_{\text{sat, obs}}$, was determined as the field at which the measured temperature gradient of the magnetization $(\partial M / \partial T)_H$ is maximized at $T = 2$ K. We estimate the expected scaling for the number of soft modes for fcc $\text{Ba}_2\text{GdSbO}_6$ on the basis of the magnon spectrum at H_{sat} derived in Ref. [18]. Error bars listed for the measured saturation field are based on the 0.2-T step size for the $M(H)$ measurements.

Compound	Lattice	N_4	$H_{\text{sat, theory}}$ (T)	$H_{\text{sat, obs}}$ (T)
$\text{Gd}_2\text{Sn}_2\text{O}_7$	Pyrochlore	N	$\frac{8J_1S}{g\mu_B} = 6.3$	5.8(2)
$\text{Gd}_3\text{Mg}_2\text{Sb}_3\text{O}_{14}$	Kagome	$\frac{2}{3}N$	$\frac{6J_1S}{g\mu_B} = 4.7$	4.6(2)
$\text{Gd}_3\text{Ga}_5\text{O}_{12}$	Garnet	$\frac{2}{3}N$	$\frac{6J_1S}{g\mu_B} = 1.7$	2.0(2)
$\text{Ba}_2\text{GdSbO}_6$	fcc	$\sim N^{1/3}$	$\frac{16J_1S}{g\mu_B} = 0.5$	1.4(2) ^a

^aAs we discuss in the main text, the temperature at which the measurement is made may be too high for the value of $H_{\text{sat, obs}}$ to be accurate in the fcc $\text{Ba}_2\text{GdSbO}_6$ case.

TABLE II. Estimated NN superexchange $J_1 = \frac{3|\Theta|}{zS(S+1)}$ and dipolar interaction $D = \frac{\mu_0 g^2 \mu_B^2}{4\pi R_{NN}^3 k_B}$ for select Gd-based frustrated magnetocaloric materials. The superexchange constant J_1 was determined from Curie-Weiss fits of the measured zero field cooled (ZFC) (1000 Oe) magnetic susceptibility χ from 8 to 50 K. Comparisons with the values reported in the literature for each compound are also provided. $J_{1,p}$ and D_p refer to the NN superexchange and dipolar term reported for the pyrochlore $\text{Gd}_2\text{Sn}_2\text{O}_7$ [26,30]. The lowest temperature of validity of the classical soft mode theory discussed in the main text is $T^* \approx J_1 S$.

	Kagome $\text{Gd}_3\text{Mg}_2\text{Sb}_3\text{O}_{14}$ ($z = 4$)		Pyrochlore $\text{Gd}_2\text{Sn}_2\text{O}_7$ ($z = 6$)		Garnet $\text{Gd}_3\text{Ga}_5\text{O}_{12}$ ($z = 4$)		fcc $\text{Ba}_2\text{GdSbO}_6$ ($z = 12$)
	Refs. [24,25]	χ^{-1} fit	Refs. [26,30]	χ^{-1} fit	Refs. [27,31]	χ^{-1} fit	χ^{-1} fit
Θ (K)	-6(1), -6.70	-6.8(1)	-9.6(1)	-8.6(1)	-2.6(1)	-2.30(1)	-0.78(1)
J_1 (K)	0.3, 0.32	0.324(5)	0.3	0.273(3)	0.107	0.110(1)	0.0124(2)
$J_1/J_{1,p}$	1	1.1	1	0.9	0.4	0.4	0.04
D (K)	0.0502		0.0496		0.0457		0.0116
D/D_p	1		1		0.9		0.2
D/J_1	0.16–0.17		0.17		0.43		0.94
T^* (K)	1		1		0.4		0.04

This is in addition to the conventional contribution to $(\partial S_m / \partial H)_T$ from the paramagnetic (unfrustrated) ordinary dispersive modes (N_2) [20] of the system:

$$\left(\frac{\partial S_m}{\partial H} \right)_{T,N_2} \propto -\frac{1}{2} \sum_{\mathbf{k}} \frac{1}{(H - H_{\text{sat}})S + \epsilon(\mathbf{k})}, \quad (3)$$

where the excitation energies $\epsilon(\mathbf{k})$ are non-negative and vanish for k corresponding to the propagation vectors of degenerate classical ground states in zero field [4].

For nonfrustrated, 3D Heisenberg magnets above the ordering temperature, $(\partial S_m / \partial H)_{T,N_2}$ is the only contribution and there is no enhancement in the magnetocaloric cooling rate, which is a temperature-independent constant for $H = H_{\text{sat}}$ [4]. In frustrated systems where N_4 is macroscopic (i.e., $N_4 \propto N$, where N is the number of lattice sites), one expects $(\partial S_m / \partial H)_{T,N_4}$ to dominate at low-enough temperatures (where it grows as approximately $1/\sqrt{T}$). However, when $N_4 \propto N^\alpha$ with $0 < \alpha < 1$, as is the case for fcc $\text{Ba}_2\text{GdSbO}_6$ (discussed below), there will always be a system size beyond which $(\partial S_m / \partial H)_{T,N_2}$ dominates, for any given temperature: $N \gtrsim 1/T^{1/[2(1-\alpha)]}$.

By classical spin-wave calculations in the saturated (collinear) state, the number of soft modes in the pyrochlore lattice was found to scale with the number of lattice sites, $N_4 \propto N$; see Table I [4]. The kagome and garnet lattices are predicted to have 2/3 as many soft modes as the pyrochlore lattice. Thus, it could be expected that the pyrochlore lattice may have a greater magnetocaloric effect than a comparable garnet or kagome lattice. Indeed prior work has shown that the pyrochlore $\text{Gd}_2\text{Ti}_2\text{O}_7$ exhibits an increased cooling rate compared with the garnet $\text{Gd}_3\text{Ga}_5\text{O}_{12}$, but that work does not address the overall magnetic entropy change (and hence total cooling) available from each material nor their differing superexchange [21].

The number of soft modes for an fcc lattice has not been reported, but it is expected to be lower than that for the corner-sharing geometries, as its zero-energy modes correspond to lines (rather than surfaces) in the Brillouin zone [22]. The appropriate scaling for the number of fcc soft modes can be predicted from the magnon spectrum at the saturation field reported in Ref. [18]:

$$\begin{aligned} \epsilon(\mathbf{q}) = 4J_1 S(1 + \cos q_x \cos q_y + \cos q_x \cos q_z \\ + \cos q_y \cos q_z). \end{aligned} \quad (4)$$

The zeros of this equation correspond to soft modes and are given by $\mathbf{q} = (\pi, q, 0)$ and the “cubic related lines” [18]. Along a given dimension of a material with N lattice sites, there are $N^{1/3}$ such \mathbf{q} states for which this is the case. Thus, the fcc lattice has a subextensive number of soft modes compared with the corner-sharing lattices.

The soft mode theory described here is valid for classical (large-spin) Heisenberg magnets [4]. The lower limit of this temperature regime, T^* , is approximated by $T^* \approx J_1 S$, below which quantum statistics must be used to analyze spin excitations [23]. Among the compounds studied, the superexchange is largest for the pyrochlore and kagome compounds, $J_1 \sim 0.3$ K in Table II, corresponding to a limiting temperature $T^* \sim 1$ K. Thus the liquid-He temperature range investigated here, 2–20 K, should provide reasonable insight into the role of soft modes in the magnetocaloric effect, as classical statistics of magnon modes apply at these temperatures.

III. EXPERIMENTAL RESULTS

A. Magnetic characterization

The measured magnetic susceptibilities of $\text{Gd}_3\text{Mg}_2\text{Sb}_3\text{O}_{14}$, $\text{Gd}_2\text{Sn}_2\text{O}_7$, $\text{Gd}_3\text{Ga}_5\text{O}_{12}$, and $\text{Ba}_2\text{GdSbO}_6$ from 1.8 to 300 K are depicted in Fig. 3. Details of sample

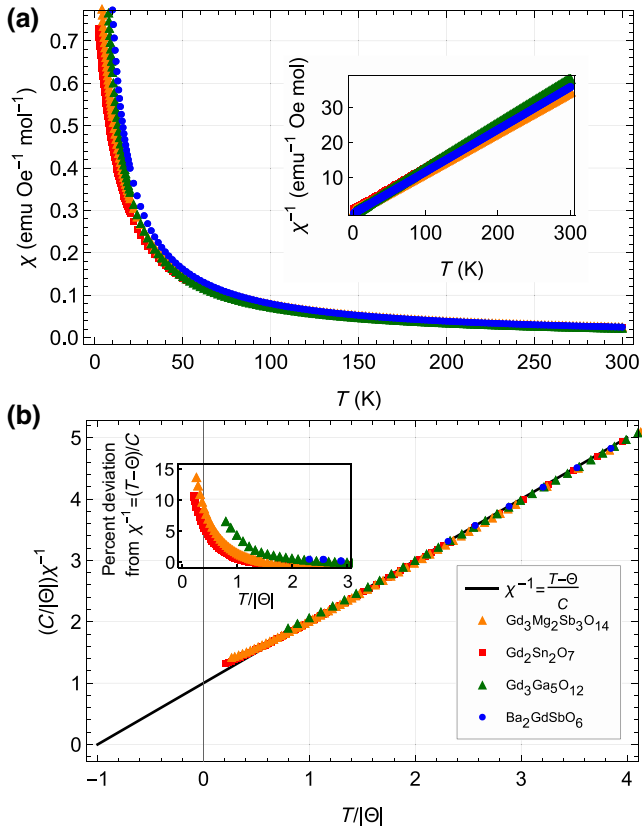


FIG. 3. (a) Measured static magnetic susceptibility χ of Gd-based kagome ($\text{Gd}_3\text{Mg}_2\text{Sb}_3\text{O}_{14}$), pyrochlore ($\text{Gd}_2\text{Sn}_2\text{O}_7$), garnet ($\text{Gd}_3\text{Ga}_5\text{O}_{12}$), and fcc ($\text{Ba}_2\text{GdSbO}_6$) compounds versus temperature (the inset shows the inverse magnetic susceptibility). (b) Dimensionless inverse magnetic susceptibility versus dimensionless temperature (the inset shows the percent deviation from the Curie-Weiss law for an enlarged region near zero temperature). Both axes are scaled with the appropriate factors of the Curie-Weiss temperature Θ and Curie constant C . All compounds exhibit positive deviations from paramagnetic behavior (black line) indicative of possible antiferromagnetic short-range correlations. The fcc lattice is effectively paramagnetic with deviations of less than 2% from Curie-Weiss behavior [15]. All measurements were made over the same temperature range, 1.8–300 K, but exhibit different dimensionless temperature ranges due to different Θ .

preparation and structural characterization can be found in Appendix F. The negative Curie-Weiss temperatures, see Table II, confirm the antiferromagnetic superexchange required for frustration and are consistent with previous literature reports [24–27]. Rearranging the Curie-Weiss law into the dimensionless form

$$\frac{C}{|\Theta|\chi} = \frac{T}{|\Theta|} + 1, \quad \Theta < 0, \quad (5)$$

where Θ is the Curie temperature and C is the Curie constant, we can compare the strength of magnetic short-range correlations between spins across different compounds

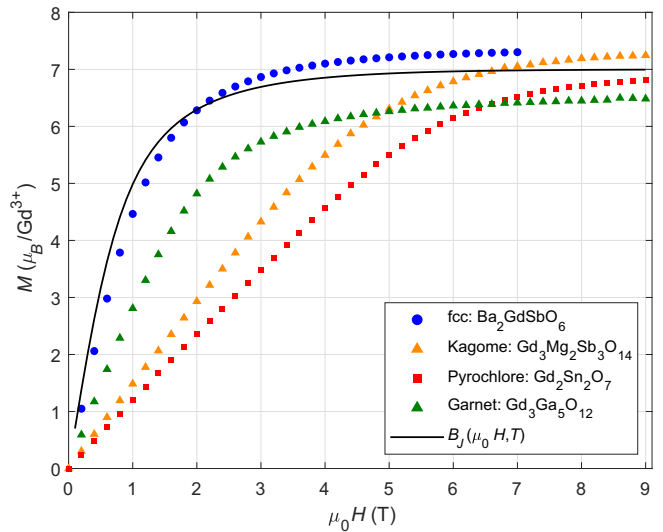


FIG. 4. Isothermal magnetization at 2 K versus applied field $\mu_0 H$ of Gd-based kagome ($\text{Gd}_3\text{Mg}_2\text{Sb}_3\text{O}_{14}$), pyrochlore ($\text{Gd}_2\text{Sn}_2\text{O}_7$), garnet ($\text{Gd}_3\text{Ga}_5\text{O}_{12}$), and fcc ($\text{Ba}_2\text{GdSbO}_6$) compounds. The solid black line gives the theoretically predicted behavior for uncoupled Heisenberg spins with $S = 7/2$.

[28]. Positive deviations from the Curie-Weiss law indicate antiferromagnetic short-range correlations, while negative deviations signify ferromagnetic correlations. As shown in Fig. 3(b), all corner-sharing geometries exhibit antiferromagnetic short-range correlations, while the fcc compound is qualitatively paramagnetic down to $T = 1.8$ K, consistent with the literature [14,15,25,29–31]. A mean-field estimate for the NN superexchange can be computed from the Curie-Weiss law using

$$J_1 = \frac{3|\Theta|}{zS(S+1)}, \quad (6)$$

where z is the number of nearest neighbors.

Table II lists the reported values for the NN superexchange J_1 and dipolar interaction D for each compound; these values are in agreement with the values obtained from the Curie-Weiss fits of the measured magnetic susceptibility in Fig. 3. Notably, J_1 is of similar magnitude for the kagome and pyrochlore compounds (approximately 0.3 K), and is about 3 and 30 times smaller for the garnet and fcc compounds, respectively. The smaller magnitude of J_1 for the fcc lattice is consistent with the minimal antiferromagnetic deviations in the dimensionless susceptibility. The dipolar interaction D in the kagome, garnet, and pyrochlore lattices is around 50 mK, and is much smaller in the fcc lattice, approximately 10 mK, due to the larger distance between nearest neighbors. The pyrochlore and kagome compounds have the lowest D/J_1 ratio, around 0.2, while the garnet compound has $D/J_1 \sim 0.4$ and the fcc lattice has $D/J_1 \sim 0.9$. Hence, the measured NN

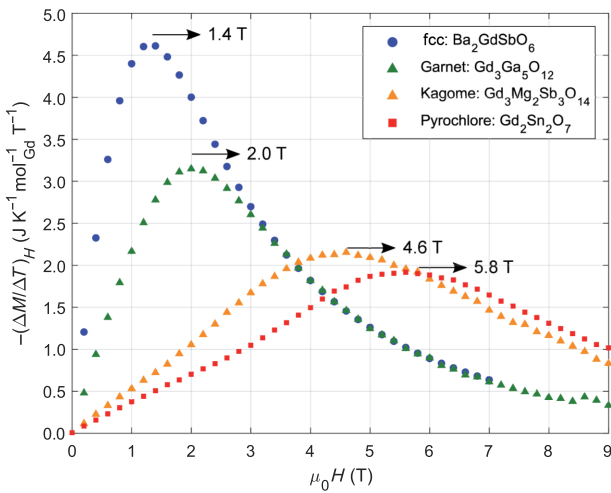


FIG. 5. Approximate magnetocaloric cooling rate $-(\Delta M/\Delta T)_H \approx -(\partial M/\partial T)_H$ versus field for $\text{Ba}_2\text{GdSbO}_6$, $\text{Gd}_3\text{Ga}_5\text{O}_{12}$, $\text{Gd}_3\text{Mg}_2\text{Sb}_3\text{O}_{14}$, and $\text{Gd}_2\text{Sn}_2\text{O}_7$ at 2 K. The values were obtained from experimental measurements of isothermal magnetization with $\Delta T = 2$ K. The resulting value of the saturation field H_{sat} for each material is indicated by the arrows.

coupling from the Curie-Weiss fit for $\text{Ba}_2\text{GdSbO}_6$ may contain contributions from dipolar interactions. For all subsequent analysis, we consider $\text{Ba}_2\text{GdSbO}_6$ to be a weakly interacting antiferromagnet, as discussed in Sec. IV.

The isothermal magnetization $M(H)$ was measured at 2 K; see Fig. 4. Within a field of 9 T, all compounds reach

a maximum value around the $7\mu_B$ per Gd^{3+} ion predicted for uncoupled Gd^{3+} Heisenberg spins. The fcc compound exhibits an isothermal magnetization that agrees well with the uncoupled Heisenberg spin prediction, owing to its small, approximately 10 mK superexchange and dipolar interactions, as shown in our prior work [15].

The saturation field of each compound was estimated from the field at which the temperature gradient of the magnetization, $-(\partial M/\partial T)_H = -(\partial S_m/\partial H)_T$, shown in Fig. 5, is maximized [4,21]. This method of estimating the saturation field should be reliable in the temperature range where spin correlations are relevant, i.e., for $T \lesssim J_1 S(S + 1)$. Theoretical predictions for H_{sat} (at zero temperature) based on the Heisenberg Hamiltonian, Eq. (1), are listed in Table I. The observed values for materials with the corner-sharing geometries agree well with the predictions, indicating that the compounds are well described by the nearest-neighbor Heisenberg model. This suggests that for $T \geq 2$ K, nearest neighbors in the paramagnetic regime superexchange J_1 play a key role in the magnetocaloric cooling rate, $(\partial S_m/\partial H)_T$. As described in Sec. IV, the fcc compound $\text{Ba}_2\text{GdSbO}_6$ can best be described as a weakly frustrated Heisenberg antiferromagnet. At 2 K, its magnetocaloric cooling rate can be modeled well with a mean-field superexchange model in the paramagnetic regime, in which spatial spin correlations are altogether ignored. Because of its small superexchange, $J_1 S(S + 1) \sim 0.2$ K, lower-temperature $M(H)$ measurements are needed to measure the saturation field with our experimental protocol. This is beyond the scope of the

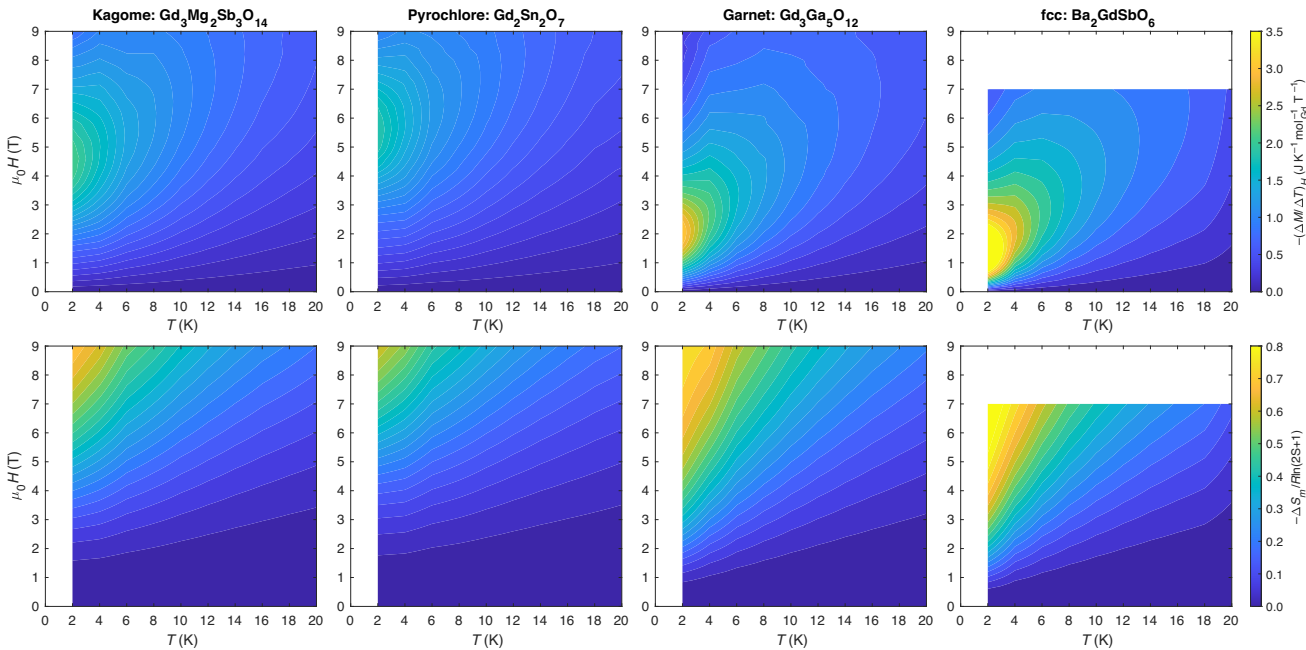


FIG. 6. Measured temperature gradient of the magnetization $-(\Delta M/\Delta T)_H \approx -(\partial M/\partial T)_H$ (with $\Delta T = 2$ K) and resulting magnetic entropy change ΔS_m , normalized by the maximum free-spin value, $R \ln(2S + 1)$, from 2 to 20 K under applied fields of 0–9 T for the Gd-based frustrated magnetocaloric materials discussed in this work.

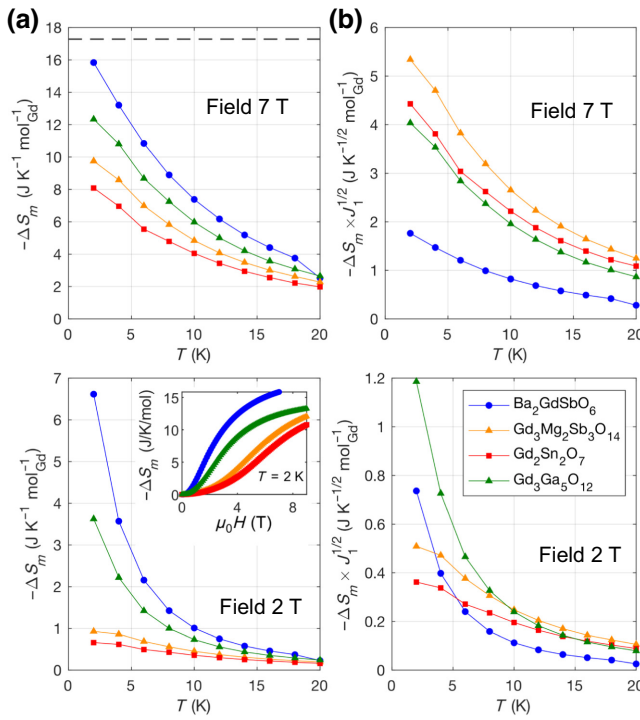


FIG. 7. (a) Magnetic entropy change ΔS_m per mole of Gd versus temperature at fields of 7 and 2 T (the inset shows ΔS_m versus the field at 2 K). The maximum possible entropy change for a paramagnetic salt, $R \ln(2S + 1)$ ($17.28 \text{ JK}^{-1} \text{ mol}^{-1}_{\text{Gd}}$), is indicated by the dashed line. (b) Superexchange-normalized magnetic entropy change $\Delta S_m \times \sqrt{J_1}$ versus temperature at fields of 7 and 2 T.

present work, and for completeness we report here the estimate of the saturation field at $T = 2 \text{ K}$, the lowest temperature measured.

B. Magnetocaloric effect

From one of Maxwell's relations, the isothermal field gradient of the magnetic entropy is related to the temperature gradient of the magnetization at constant field via $(\partial S_m / \partial H)_T = (\partial M / \partial T)_H$. Thus, the magnetic entropy change, ΔS_m , can be measured using the isothermal magnetization via

$$\Delta S_m(T_0, H_{\max}) = \int_0^{H_{\max}} \left(\frac{\partial M(T, H)}{\partial T} \right)_H \Big|_{T=T_0} dH. \quad (7)$$

The magnetic entropy change ΔS_m of each Gd-based compound was measured from 2 to 20 K in fields of up to 9 T from the isothermal magnetization; see Figs. 6 and 7(a). The magnetization data were measured in temperature steps of 2 K, and thus we are able to measure the finite difference ratio $(\Delta M / \Delta T)_H$ only as an estimate for the magnetocaloric cooling rate $(\partial M / \partial T)_H$ prior to computing the magnetic entropy change via Eq. (7) (see Appendix D).

Per mole of Gd, the maximum entropy change attainable for a paramagnetic salt is $R \ln(2S + 1)$ ($17.28 \text{ JK}^{-1} \text{ mol}^{-1}_{\text{Gd}}$). We find that the fcc $\text{Ba}_2\text{GdSbO}_6$ exhibits the greatest magnetic entropy change $-\Delta S_m$, reaching $0.9R \ln(2S + 1)$ in a field of just 7 T at 2 K. On the other hand at 2 K and a larger field of 9 T, the corner-sharing geometries exhibit entropy changes of $0.8R \ln(2S + 1)$, $0.7R \ln(2S + 1)$, and $0.6R \ln(2S + 1)$ for the garnet, kagome, and pyrochlore lattices, respectively. At a low field of 2 T, the fcc and garnet compounds are still the best performing, with $-\Delta S_m$ of $0.4R \ln(2S + 1)$ and $0.2R \ln(2S + 1)$, respectively, compared with approximately $0.05R \ln(2S + 1)$ for the kagome and pyrochlore compounds; see Fig. 7(a). Despite having the largest number of soft modes, the pyrochlore material achieves the smallest magnetic entropy change per Gd³⁺ ion.

IV. DISCUSSION

The enhanced performance of the fcc $\text{Ba}_2\text{GdSbO}_6$ and garnet $\text{Gd}_3\text{Ga}_5\text{O}_{12}$ compared with the pyrochlore $\text{Gd}_2\text{Sn}_2\text{O}_7$ is at first surprising, given the reduced number of soft modes (Table I). However, from Eqs. (2) and (3) we see that the measured magnetocaloric cooling rate results from two different contributions, one due to the number of soft modes N_4 (frustrated response) and one due to ordinary dispersive modes N_2 (paramagnetic response). To investigate this in greater detail, we compare the experimental data with mean-field modeling [15] and classical Heisenberg Monte Carlo simulations of the finite difference ratio $-(\Delta M / \Delta T)_H$ for each of the four systems (see Fig. 8). For reference, we show in Fig. 10 in Appendix B a comparison between the finite difference ratio $-(\Delta M / \Delta T)_H$ and the exact magnetocaloric effect $-(\partial S_m / \partial H)_T = -(\partial M / \partial T)_H$ for the mean-field results and the Monte Carlo results. Details for the Monte Carlo simulations can be found in Appendix C.

Our results show that the fcc compound is described quantitatively well in the paramagnetic regime by the mean-field NN superexchange model [15] across the full range of temperatures of interest in this study [32]. This finding suggests that the paramagnetic response dominates for this compound in the temperature and field regime of interest. We recall indeed that the fcc lattice is predicted to have only a subextensive number of soft modes, and therefore the contribution $(\partial S_m / \partial H)_{T, N_4}$ at the saturation field becomes irrelevant in the thermodynamic limit. The paramagnetic term $(\partial S_m / \partial H)_{T, N_2}$ is expected to be the dominant contribution to the measured magnetic entropy change ΔS_m .

In contrast, for the other three (corner-sharing) compounds we clearly see an increasing discrepancy between the mean-field results and in the experimental results at lower temperatures (2 and 4 K). This is consistent with the 10–30-fold larger values of J_1 in these systems,

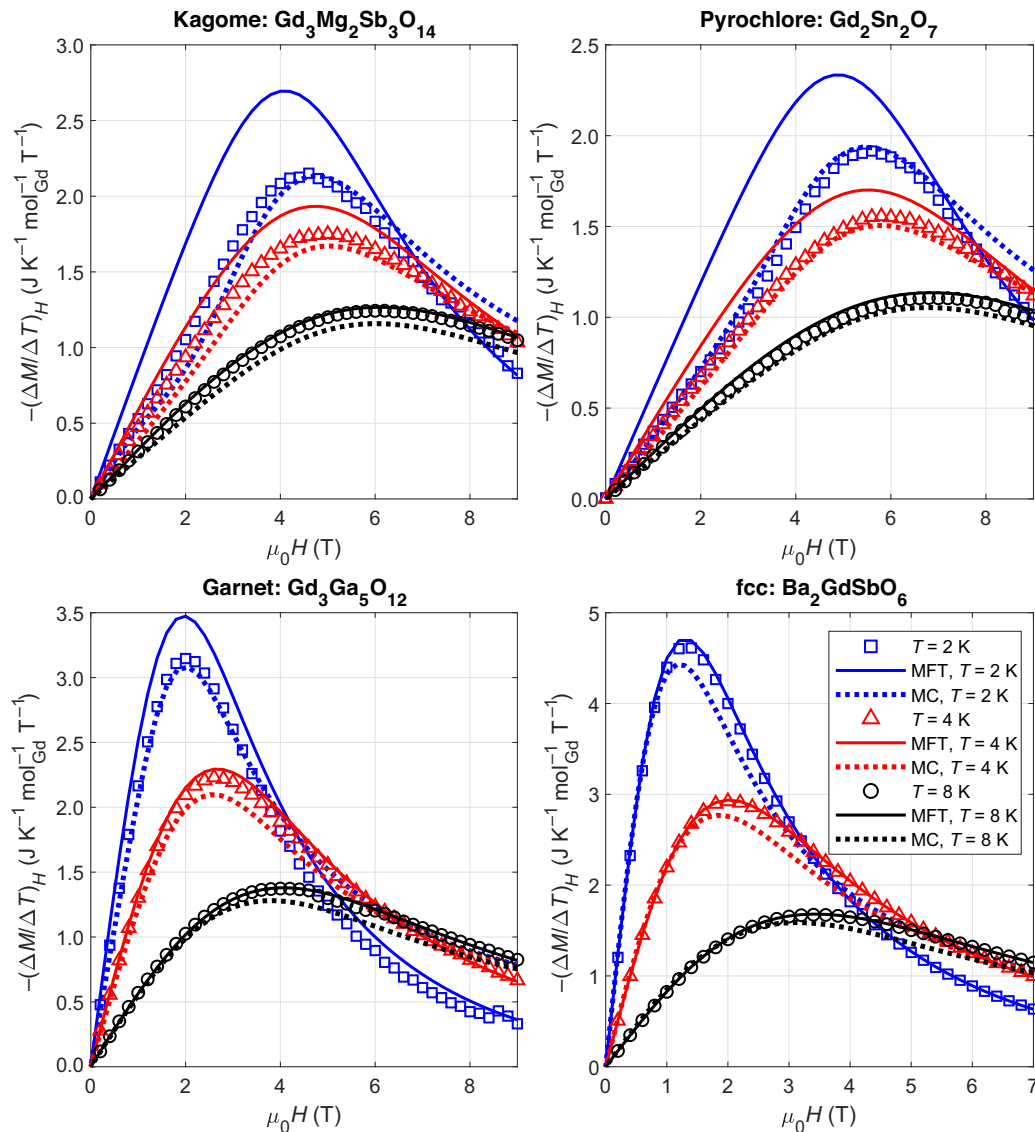


FIG. 8. Approximate magnetocaloric cooling rate $-(\Delta M / \Delta T)_H \approx -(\partial M / \partial T)_H = -(\partial S_m / \partial H)_T$ extracted from the measured isothermal magnetization with $\Delta T = 2 \text{ K}$ (data points) compared with predictions based on the magnetization M for Heisenberg $S = 7/2$ spins in the mean-field superexchange model (MFT) (solid lines) and classical Monte Carlo simulations (MC) (dotted lines). These results show that the fcc compound is well described by mean-field quantum spins, which ignore spatial correlations. Conversely, the better agreement of the classical Monte Carlo simulations for the corner-sharing geometries highlights the importance of magnetic correlations in those compounds.

resulting in correspondingly stronger correlations. The latter are generally expected to have two effects: (1) to reduce the N_2 contribution to the magnetocaloric effect (the spins have reduced ability to fluctuate independently of one another) and (2) to give rise to an extensive number of frustrated collective soft modes N_4 , which contribute with a prefactor scaling as $1/\sqrt{T}$ to $(\partial S_m / \partial H)_T$. The comparatively better agreement of the experimental curves with classical Monte Carlo simulations, with respect to the mean-field results, demonstrates how the simulations are able to capture both the paramagnetic contribution and the soft mode

contribution, with corrections at large fields due to quantization effects [33].

Our having established the importance of soft modes in the magnetocaloric performance of the corner-sharing geometries, it remains to be seen why the garnet lattice outperforms both the pyrochlore lattice and the kagome lattice. This can be explained by the fact that the measured entropy changes in Figs. 6 and 7(a) do not account for differences in the value of the superexchange coupling J_1 . To account for the role of superexchange in the predicted enhancement at the saturation field, Eq. (2), the magnetic entropy maps were scaled by $\sqrt{J_1}$; see Figs. 7(b)

and 9. While the soft mode contribution to the magnetic entropy change is expected to vanish for the fcc lattice due to its subextensive N_4 , we include Ba₂GdSbO₆ for ease of comparison. After normalization, the pyrochlore lattice becomes the top performer among the 3D geometries at 7 T, as predicted by Ref. [4], while the kagome lattice is the top performer overall.

The experimental variations of the magnetic entropy normalized by the superexchange value for each material, $-\sqrt{J_1}\Delta S_m$, agrees with the qualitative behavior predicted by the soft model analysis. From Eq. (2), the maximum in $(\partial S_m/\partial H)_T$ at the saturation field H_{sat} should scale proportionally to the number of soft modes N_4 , once normalized by the square root of the superexchange $\sqrt{J_1}$. This qualitative agreement is striking as it reproduces the predicted ranking for the 3D frustrated lattices of the pyrochlore compound ($N_4 \sim N$), followed by the garnet compound ($N_4 \sim 2N/3$), and then the fcc compound ($N_4 \sim N^{1/3}$) for applied fields greater than or equal to saturation (i.e., $H \geq 5.8$ T). At the low field of 2 T, the kagome and pyrochlore compounds are not fully saturated, explaining why, as might be expected, the garnet and fcc lattices exhibit the greatest $-\sqrt{J_1}\Delta S_m$; see Fig. 7(b). A more quantitative assessment of the agreement with the model at lower fields is not possible, likely due to other minor contributions (e.g., dipole-dipole interactions and disorder), which were not accounted for in our study.

The implication of this experimental validation is that while the order of soft modes of frustrating lattices can be accurately captured in experiments, soft modes are not the leading contribution in the magnetocaloric performance of a frustrated magnet in the liquid-He regime. Rather, as demonstrated in Figs. 6 and 7, materials with the smallest superexchange (i.e., the fcc and garnet compounds) exhibit the greatest performance, as the paramagnetic contribution to the entropy change is not constrained by short-range correlations, so spins can fluctuate independently of one another. It is conceivable that at lower temperatures relative to the superexchange J_1 (much less than 2 K), soft modes may become the determining factor in the magnetocaloric effect. However, such low temperatures would soon require a revision of the model to include quantum statistics to study spin excitations.

Another interesting result from this study is that in the limit where superexchange determines the magnetocaloric cooling rate, differences between the pyrochlore and kagome lattices are not predicted by the model. In this case, they may arise from the presence of site disorder [10.5(2)%] in Gd₃Mg₂Sb₃O₁₄ (Appendix F) relieving frustration, or spin anisotropies not included in this analysis, which applies only to isotropic Heisenberg spins.

This study has focused on four frustrated oxides. However, there are many other magnetic lattices where a high magnetocaloric effect is reported, including the 2D triangular (GdBO₃ [34]) and Shastry-Sutherland (Gd₂Be₂GeO₇

[35]) lattices and quasi-1D spin chains [Gd(HCOO)₃, GdOHCO₃, Ca₄GdO(BO₃)₃ [8,36,37]]. In many of these systems, the presence of polyanions (BO₃³⁻, HCOO⁻, etc.) or molecular ligands may complicate the soft mode analysis presented in Ref. [4] due to changes in the hydrogen bonding or other molecular interactions [38,39]. Magnetostructural coupling, which results in changes in the structure, phonon properties, and electronic properties on application of a magnetic field, as reported in the high-temperature magnetocaloric measurements on MnB [40], will also result in more complex magnetocaloric behavior. Such materials are beyond the scope of this initial study. Future work could incorporate the soft mode analysis of other geometrically frustrated magnetic lattices, e.g., edge-sharing motifs such as the edge-sharing triangles in a honeycomb arrangement in SrLn₂O₄ [41].

The mean-field nature of the analysis conducted here is applicable only to Heisenberg spins. However, we note that on the basis of literature reports, the magnetic and magnetocaloric properties of all four magnetic lattices studied here vary significantly for lanthanide ions with nonzero angular momentum, L [13,15,42–48]. Anisotropic magnetic systems such as those based on Dy³⁺ ($4f^9$, $L = 5$, $J = 15/2$, $S = 5/2$, and $g_J = 4/3$) have been found as useful magnetocaloric candidates at low fields (e.g., $\mu_0 H \leq 2$ T), compared with the Gd³⁺ counterparts. For example, the magnetic entropy change of Ising garnet Dy₃Ga₅O₁₂ reaches 4 times that in the Heisenberg Ga₃Ga₅O₁₂ for a 1 T field at 2 K [42]. Adiabatic temperature measurements have shown that the Ising spin ice Dy₂Ti₂O₇ can cool from approximately 1 K to 0.3 K in a field of just 0.8 T, while Gd₂Ti₂O₇ requires a field of approximately 9 T to cool to 0.5 K from the same starting temperature [44,45]. Extending this analysis to anisotropic systems is an interesting avenue for future research, likely requiring nontrivial microscopic modeling of the single-ion anisotropy.

These results suggest that future research for cryogenic magnetic refrigeration should focus on frustrated magnets with the smallest superexchange. The strategy of solely reducing the exchange by increasing the distance between magnetic ions, as in the dilute magnetic salts ferric ammonium alum and cerous magnesium nitrate, is not effective. When the four materials studied here are normalized by volume and mass, see Appendix E, the fcc lattice is the poorest performer despite having the weakest superexchange coupling. This highlights the importance of reducing J_1 while maintaining a dense magnetic lattice [15]. Furthermore, in these dense lattices, soft modes could provide an additional cooling mechanism at lower temperatures.

V. CONCLUSION

This work examines the role of lattice geometry in maximizing the magnetocaloric effect via soft mode

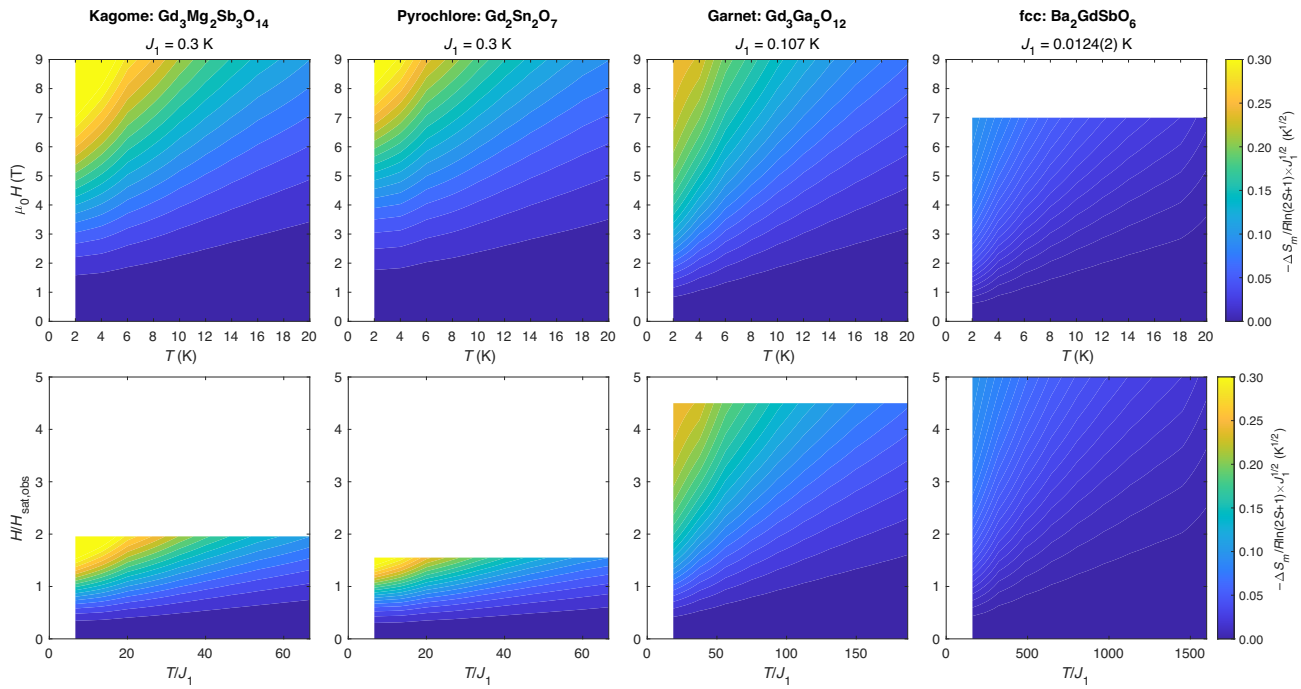


FIG. 9. Measured magnetic entropy change normalized by the NN superexchange, $\Delta S_m \times \sqrt{J_1}$. When we account for the differences in the superexchange term, the pyrochlore lattice becomes the best performing among the 3D frustrated lattices. The top row shows $\Delta S_m \times \sqrt{J_1}$ as a function of absolute temperature T and applied field $\mu_0 H$, while the bottom row has the temperature axis rescaled by J_1 and the field axis rescaled by the observed saturation field $\mu_0 H_{\text{sat,obs}}$ for each compound.

spin excitations. Four representative Heisenberg (3D, Gd-based) spin systems were investigated, including the three corner-sharing garnet ($\text{Gd}_3\text{Ga}_5\text{O}_{12}$), pyrochlore ($\text{Gd}_2\text{Sn}_2\text{O}_7$), and kagome ($\text{Gd}_3\text{Mg}_2\text{Sb}_3\text{O}_{14}$) lattices and the edge-sharing fcc lattice ($\text{Ba}_2\text{GdSbO}_6$). For the liquid-He temperature range investigated (2–20 K), magnetic entropy change measurements indicate that the smaller superexchange of the fcc and garnet lattices allows better magnetocaloric performance than the strongly coupled pyrochlore analogue, despite its larger number of soft modes. Our results show that a paramagnetic response dominates over geometric frustration in enhancing the magnetocaloric effect. However, the contribution to the magnetocaloric effect in systems with an extensive number of frustrated magnetic soft modes is expected to take over at lower temperatures, thus providing an additional channel for maximizing the magnetocaloric effect in highly frustrated magnetic lattices. Our results highlight the importance of the magnetic lattice geometry and its role in the observed magnetocaloric effect. Future magnetocaloric material design should focus on both the superexchange and the magnetic lattice to optimize the trade-off between spin polarizability and frustrated soft mode enhancement.

Data associated with this publication can be found online [49].

ACKNOWLEDGMENTS

This work was supported by the UK Engineering and Physical Sciences Research Council (EPSRC) grants (Grants No. EP/P034616/1, No. EP/V062654/1, and No. EP/T028580/1) and the Winton Programme for the Physics of Sustainability. E.C.K. gratefully acknowledges the support of a Churchill Scholarship from the Winston Churchill Foundation of the United States. M.E.Z. acknowledges financial support from the French Agence Nationale de la Recherche (Grant No. ANR-18-CE05-0023). Magnetic measurements were made on the EPSRC Advanced Characterization Suite (Grant No. EP/M0005/24/1).

APPENDIX A: SATURATION FIELD OF THE fcc MODEL

One can use frustrated block decomposition to obtain the saturation field H_{sat} for the nearest-neighbor fcc antiferromagnet, above which spins become fully aligned with the applied field. We start with the spin Hamiltonian

$$\mathcal{H} = J_1 \sum_{\langle ij \rangle} \mathbf{S}_i \cdot \mathbf{S}_j - H \sum_i S_i^z, \quad (\text{A1})$$

where the $g\mu_B$ prefactor in the Zeeman term has been absorbed into H . An fcc lattice can be represented as an edge-sharing arrangement of tetrahedra, which are labeled by an index α . Introducing the tetrahedron magnetization $\mathbf{L}_\alpha = \sum_{i \in \alpha} \mathbf{S}_i$, and using the fact that every site belongs to eight tetrahedra, one can show that

$$\sum_i S_i^z = \frac{1}{8} \sum_\alpha L_\alpha^z. \quad (\text{A2})$$

Similarly, since every NN bond of the fcc lattice belongs to two tetrahedra, we find that

$$\sum_{\langle ij \rangle} \mathbf{S}_i \cdot \mathbf{S}_j = \frac{1}{4} \sum_\alpha (\mathbf{L}_\alpha)^2 + \text{const.} \quad (\text{A3})$$

The Hamiltonian (A1) can be now rewritten, up to an irrelevant constant, as

$$\begin{aligned} \mathcal{H} &= \frac{1}{4} \sum_\alpha \left[J_1 \mathbf{L}_\alpha^2 - \frac{H}{2} L_\alpha^z \right] \\ &= \frac{J_1}{4} \sum_\alpha \left[\mathbf{L}_\alpha - \frac{H\hat{z}}{4J_1} \right]^2 + \text{const.} \end{aligned} \quad (\text{A4})$$

For a single tetrahedron, the energy is minimized when $\mathbf{L}_\alpha = (H/4J_1)\hat{z}$. If this condition can be met for *all tetrahedra simultaneously*, then it is the lowest-energy state of the system and its zero-temperature state.

Because $|\mathbf{S}_i| = S$, L_α^z is upper bounded by the maximum possible value $(L_\alpha^z)_{\max} = 4S$, if $H > 16J_1S$, then the minimum-energy condition cannot be achieved and the lowest-energy state corresponds the uniformly polarized spin configuration. This value is referred to as the “saturation field,”

$$g\mu_B H_{\text{sat}} = 16J_1S. \quad (\text{A5})$$

APPENDIX B: MEAN-FIELD APPROXIMATION

A mean-field approximation (random-phase approximation) [15,25] was used to estimate the paramagnetic contribution to the magnetocaloric cooling rate $(\partial S_m / \partial H)_T$ for each compound, with the interactions truncated at nearest-neighbor distance. The antiferromagnetic coupling between $S = 7/2$ spins amounts to an exchange field, \mathbf{H}_{exc} , which adds to the external field, \mathbf{H}_{ext} , to produce the net field, \mathbf{H}_{tot} , experienced by a single spin.

Note that dipolar interactions can be ignored for the corner-sharing lattice compounds considered in this study since they are weak in comparison with the nearest-neighbor exchange (see Table II). This is not the case for the fcc material. However, the contribution of dipolar interactions for a cubic Bravais lattice vanishes identically in

TABLE III. Mean-field saturation magnetization parameter M_{sat} determined by our fitting the observed saturation magnetization, as well as the NN superexchange J_1 , for each compound, and R^2 of the fit.

Compound	M_{sat} (gS)	Fit J_1 (K)	R^2
$\text{Gd}_3\text{Mg}_2\text{Sb}_3\text{O}_{14}$	1.0268	0.312(3)	0.9982
$\text{Gd}_2\text{Sn}_2\text{O}_7$	0.9744	0.273(2)	0.9976
$\text{Gd}_3\text{Ga}_5\text{O}_{12}$	0.9257	0.114(1)	0.9997
$\text{Ba}_2\text{GdSbO}_6$	1.04	0.0113(3)	1.0000

the case of a (uniform) mean-field approximation, due to rotational lattice symmetry.

Since $L = 0$ for Gd^{3+} , the exchange constant J_1 can be assumed to be isotropic, so the exchange field is given by

$$\mathbf{H}_{\text{exc}} = a_{\text{ex}} z M \hat{\mathbf{H}}_{\text{ext}} = \frac{-J_1}{g^2 \mu_B} z M \hat{\mathbf{H}}_{\text{ext}}, \quad (\text{B1})$$

where M is the bulk magnetization in units of the Bohr magneton and a_{ex} is the “field parameter” in units of the magnetic field [25]. The bulk magnetization of the system at a given temperature T and external field H_{ext} is given by the solutions of the transcendental self-consistency equation

$$M - gSB_S(|\mathbf{H}_{\text{tot}}(M)|, T) = 0, \quad (\text{B2})$$

where B_S is the Brillouin function given by

$$B_S(y) = \frac{2S+1}{2S} \coth\left(\frac{2S+1}{2S}y\right) - \frac{1}{2S} \coth\left(\frac{y}{2S}\right), \quad (\text{B3})$$

with $y = \mu_0 H g \mu_B S / (k_B T)$, where $H = |\mathbf{H}_{\text{tot}}|$ [25].

As a further consistency check, we leave J_1 as a free parameter in our model. Global least-squares fits to the measured isothermal magnetization $M(H)$ (2–20 K) using Eq. (B2) were used to determine the NN superexchange J_1 in $\text{Ba}_2\text{GdSbO}_6$, $\text{Gd}_2\text{Sn}_2\text{O}_7$, $\text{Gd}_3\text{Ga}_5\text{O}_{12}$, and $\text{Gd}_3\text{Mg}_2\text{Sb}_3\text{O}_{14}$. The fit J_1 values, Table III, are in agreement with the values reported in the literature and Curie-Weiss fits; see Table II. The free-spin magnetization $M_{S=7/2} = gSB_S(|\mathbf{H}_{\text{ext}}|, T)$ was used as an initial guess to solve iteratively the mean-field self-consistency condition, Eq. (B2). The observed saturation value of the magnetization at the maximum field can vary due to experimental uncertainty, so all compounds were fit with a scaled fraction of $M_{\text{sat}} = gS$ to match the observed value; see Table III.

The approximate magnetocaloric cooling rate $(\Delta M / \Delta T)_H$ was then calculated from the model predictions of $M(H)$ using the fit NN superexchange constants J_1 , Eq. (D1), at the same resolution as the experimental data (i.e., $\Delta T = 2$ K). In the limit

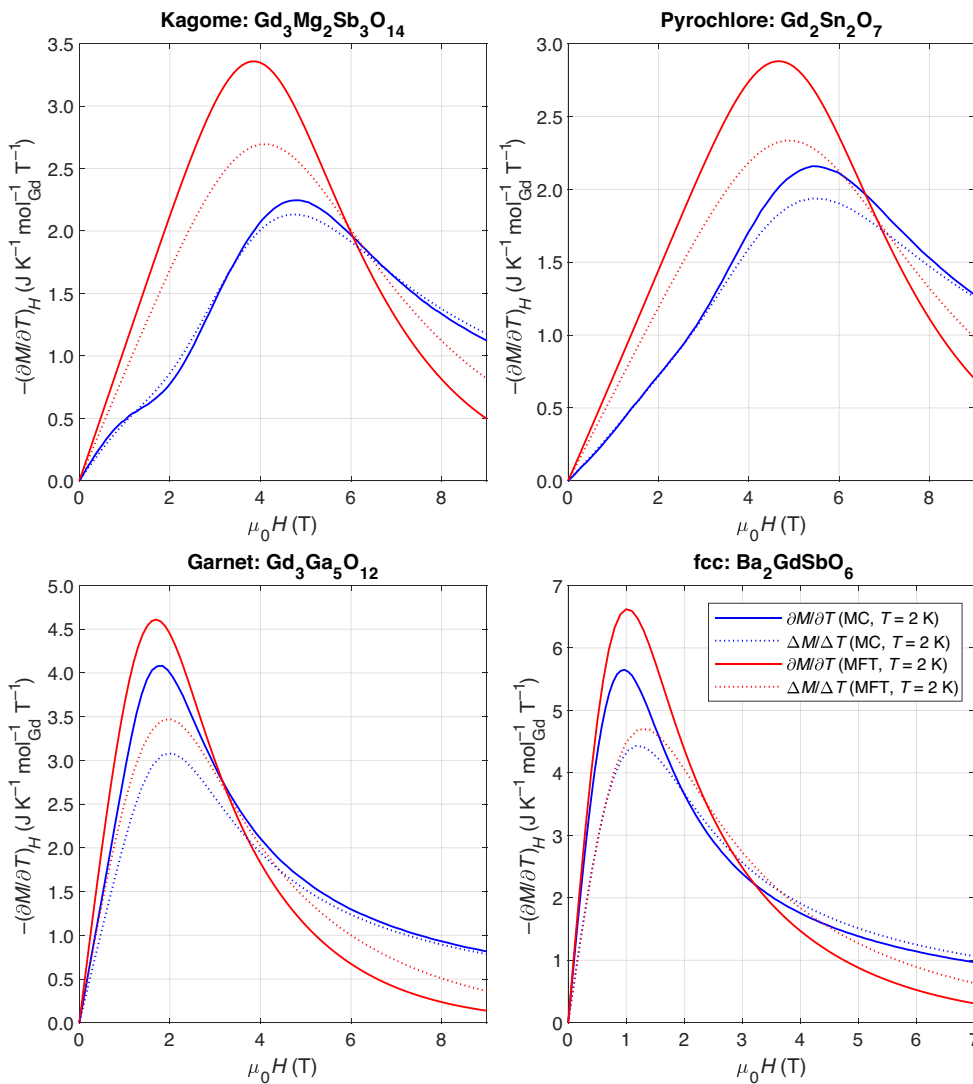


FIG. 10. Comparison of the exact, $-(\partial S_m / \partial H)_T = -(\partial M / \partial T)_H$, versus the approximate, $-(\Delta M / \Delta T)_H$ with $\Delta T = 2 \text{ K}$, magnetocaloric cooling rates for the four frustrated geometries obtained classical Monte Carlo simulations (MC) (blue lines) and mean-field theory (MFT) (red lines) at $T = 2 \text{ K}$. Exact magnetocaloric cooling rates are shown as solid lines, while approximate rates are shown as dotted lines.

that $\Delta T \rightarrow 0$, one recovers the exact magnetocaloric cooling rate, $\lim_{\Delta T \rightarrow 0} (\Delta M / \Delta T)_H = (\partial M / \partial T)_H$. A comparison between the exact magnetocaloric cooling rate and the approximate magnetocaloric cooling rate obtained from mean-field theory is shown in Fig. 10 for all four materials (computed via a converged numerical derivative with $\Delta T = 0.001 \text{ K}$).

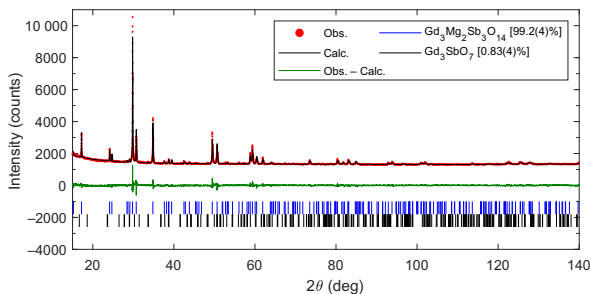


FIG. 11. Rietveld refinement of $\text{Gd}_3\text{Mg}_2\text{Sb}_3\text{O}_{14}$ from powder XRD.

APPENDIX C: MONTE CARLO SIMULATIONS

The classical Monte Carlo simulations were performed on periodic lattices with 2000–4000 spins. Since in the temperature range studied all materials remain in the paramagnetic state, the simulated system sizes are sufficient to obtain the bulk behavior without additional finite-size scaling. We simulated the nearest-neighbor antiferromagnetic model

$$\hat{\mathcal{H}}_c = \sum_{\langle ij \rangle} \mathbf{s}_i \cdot \mathbf{s}_j - \mathbf{H} \cdot \sum_i \mathbf{s}_i, \quad (\text{C1})$$

where the spins \mathbf{s}_i are classical vectors of unit length, $|\mathbf{s}_i| = 1$. A hybrid Monte Carlo algorithm was used with canonical Metropolis sweeps over the lattice followed by microcanonical over-relaxation steps. At each temperature/field point, 10^4 Metropolis steps were used for equilibration, with subsequent 10^5 hybrid Monte Carlo steps for measurements. In addition, we performed averaging over 100

TABLE IV. Measured magnetocaloric effect at $T = 2$ K and $\mu_0 H = 9$ T for the corner-sharing geometries and at $T = 2$ K and $\mu_0 H = 7$ T for the fcc lattice, normalized by volume and by mass. Mass densities ρ were determined from Rietveld refinement for the kagome, garnet, and fcc lattices (see Appendix F) and from the value reported in the literature for the pyrochlore lattice [53].

Compound	ΔS_m (JK ⁻¹ mol ⁻¹ _{Gd})	Molar mass (g mol ⁻¹)	ρ (g cm ⁻³)	ΔS_m (mJ K ⁻¹ cm ⁻³)	ΔS_m (mJ K ⁻¹ kg ⁻¹)
Gd ₃ Mg ₂ Sb ₃ O ₁₄	$0.71R \ln(2S + 1)$	1109.63	6.75	220	33
Gd ₂ Sn ₂ O ₇	$0.62R \ln(2S + 1)$	663.92	7.72	250	32
Gd ₃ Ga ₅ O ₁₂	$0.77R \ln(2S + 1)$	1012.36	7.09	280	39
Ba ₂ GdSbO ₆	$0.92R \ln(2S + 1)$	649.66	7.09	170	24

independent Monte Carlo runs. Relative statistical errors do not exceed 0.5% for all quantities obtained.

The approximate magnetocaloric cooling rate ($\Delta M / \Delta T)_H$ was computed from the magnetization using the finite difference method, Eq. (D1), at the resolution of the experimental data (i.e., temperature steps of 2 K). The exact magnetocaloric cooling rate ($\partial M / \partial T)_H$ was computed from the energy-magnetization cumulant:

$$\left(\frac{\partial S_m}{\partial H}\right)_T = \left(\frac{\partial M}{\partial T}\right)_H = \frac{1}{T^2} \left(\langle EM \rangle - \langle E \rangle \langle M \rangle \right), \quad (C2)$$

where $\langle \dots \rangle$ denotes statistical averaging. Figure 10 shows a comparison between the exact and approximate values for reference. It also allows a comparison between the classical Monte Carlo results and the mean-field modeling in Appendix B; the enhanced magnetocaloric effect in the latter is likely due to the quantized nature of the spins.

Rescaling between dimensionless values obtained from the classical Monte Carlo simulations [Eq. (C1)] and real physical properties of each material was done with the

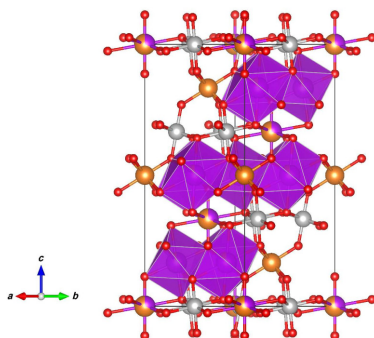


FIG. 12. Refined crystal structure of Gd₃Mg₂Sb₃O₁₄. The compound exhibits some site disorder, with 10.5(2)% of Mg²⁺ ions from the 3a site lying on the kagome Gd³⁺ 9d site: see Table V. Gd³⁺ ions and corresponding O polyhedra are shown in purple, Mg²⁺ ions are shown in orange, Sb⁵⁺ ions are shown in gray, and O²⁻ ions are shown in red. This figure was generated from the refined crystal structure file with use of VESTA [56].

conversion factors

$$\begin{aligned} \mu_0 H_{\text{expt.}} &= \frac{J_1 S}{g \mu_B} H_{\text{MC}}, \quad k_B T_{\text{expt.}} = J_1 S (S + 1) T_{\text{MC}}, \\ \left(\frac{\partial M}{\partial T}\right)_{\text{expt.}} &= \frac{g \mu_B N_A}{J_1 (S + 1)} \left(\frac{\partial M}{\partial T}\right)_{\text{MC}}. \end{aligned} \quad (C3)$$

Here $S = 7/2$ and $g \approx 2$ are the spin and the g factor of Gd³⁺ ions, J_1 is the nearest-neighbor exchange, k_B is the Boltzmann constant, and N_A is the Avogadro number.

APPENDIX D: EXPERIMENTAL METHODS

1. Sample preparation

Polycrystalline samples were prepared by a solid-state method consistent with prior reports in the literature [15, 24, 27, 30]. Reactants oxides were ground with use of a mortar and pestle and then heated in air in an alumina crucible at $T \sim 1300^\circ\text{C}$ for several days with intermittent grindings to ensure a complete reaction. As described in Appendix F, x-ray diffraction (XRD) indicates phase pure samples (less than 1 wt % impurities of Gd₃SbO₇ in Ba₂GdSbO₆) with crystal structures consistent with the values reported in the literature.

2. X-ray diffraction and crystal structure refinements

Room-temperature powder XRD measurements were conducted with a Bruker D8 Advance diffractometer (Cu $K\alpha$ radiation, $\lambda = 1.54$ Å). Data were collected with

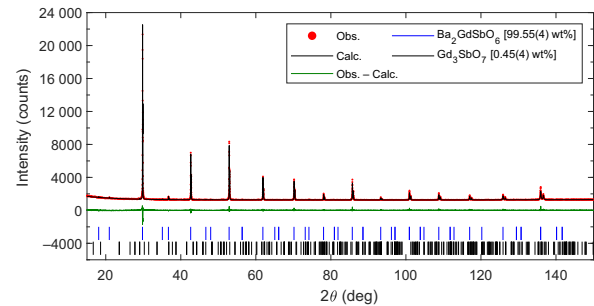
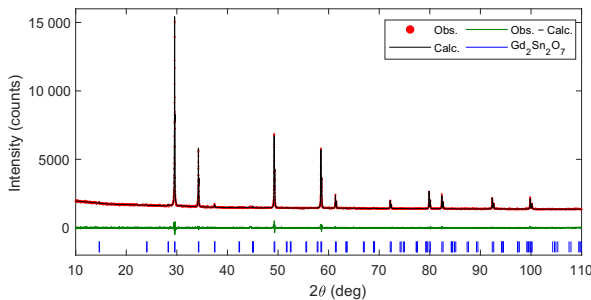


FIG. 13. Rietveld refinement of Ba₂GdSbO₆ from powder XRD.

FIG. 14. Rietveld refinement of $\text{Gd}_2\text{Sn}_2\text{O}_7$ from powder XRD.

$d(2\theta) = 0.01^\circ$ from $2\theta = 15^\circ$ to $2\theta = 150^\circ$, with an overall collection time of 2–3 h. Rietveld refinements [50] of the powder XRD data were done with DIFFRAC.SUITE TOPAS5 [51]. The background was modeled with a 13-term Chebyshev polynomial and peak shapes were fit with a pseudo-Voigt function [52]. All Debye-Waller factors were set constant to the values reported in the literature.

3. Bulk magnetic measurements

Bulk magnetic measurements of the magnetic susceptibility $\chi(T) = dM/dH$ were conducted with a Quantum Design magnetic properties measurement system (MPMS) with a superconducting interference device (SQUID). Susceptibility measurements were made at $\mu_0H = 0.01$ T, in the low-field limit where $\chi(T) = dM/dH \approx M/H$ in zero-field-cooled conditions from 1.8 to 300 K. $M(H)$ measurements (described below) were linear at this field, confirming that this linear approximation of χ is valid. Isothermal magnetization $M(H)$ was measured with the ACMS option of a Quantum Design physical properties measurement system (PPMS) for $\text{Gd}_3\text{Mg}_2\text{Sb}_3\text{O}_{14}$, $\text{Gd}_3\text{Ga}_5\text{O}_{12}$, and $\text{Gd}_2\text{Sn}_2\text{O}_7$ and a Quantum Design MPMS SQUID for $\text{Ba}_2\text{GdSbO}_6$. $M(H)$ measurements were made at temperatures of 2–22 K in steps of 2 K over a field range of 0–9 T in steps of 0.2 T (up to only 7 T for $\text{Ba}_2\text{GdSbO}_6$).

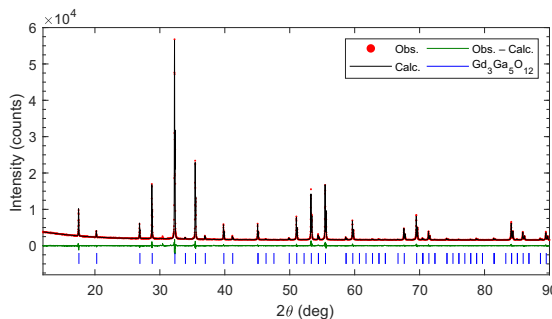
FIG. 15. Rietveld refinement of $\text{Gd}_3\text{Ga}_5\text{O}_{12}$ from powder XRD.

TABLE V. Structural parameters of $\text{Gd}_3\text{Mg}_2\text{Sb}_3\text{O}_{14}$. Powder XRD refinements were performed in the space group $R\bar{3}m$, with Mg(1) on the $3a$ sites $(0, 0, 0)$, Mg(2) on the $3b$ sites $(0, 0, 1/2)$, Gd(1) on the $9d$ sites $(1/2, 0, 1/2)$, Sb on the $9e$ sites $(1/2, 0, 0)$, O(1) on the $6c$ sites $(0, 0, z)$, and O(2) and O(3) on the $18h$ sites (x, \bar{x}, z) . Partial occupancy between the $3a$ and $9d$ sites was also refined according to the formula $[\text{Gd}(1)_{1-x}\text{Mg}(3)_x]_{9d}[\text{Mg}(1)_{1-3x}\text{Gd}(2)_{3x}]_{3a}$ as in Ref. [54].

Parameter	Value	
a (Å)	7.3634(1)	
c (Å)	17.4511(3)	
Mg(1)/Gd(2) ($3a$)	Occupancy	0.686(6), 0.314(6)
Gd(1)/Mg(3) ($9d$)	Occupancy	0.895(2), 0.105(2)
O(1)	z	0.113(1)
O(2)	x	0.5261(7)
	z	0.8974(6)
O(3)	x	0.4714(8)
	z	0.3591(5)
Overall B_{iso} (Å 2)	0.76(2)	
Gd_3SbO_7 (wt %)	0.83(4)	
R_{wp}	9.69	
χ^2	1.42	

4. Magnetocaloric effect calculations

The magnetic entropy change for a field H_{max} relative to zero field was calculated from the measured $M(H)$ by our first computing the temperature derivative of the magnetization using the finite differences approximation,

$$\left(\frac{\partial M(T, H)}{\partial T} \right)_{H=T_i} \Big|_{T=T_i} \approx \frac{M(T_{i+1}, H) - M(T_i, H)}{T_{i+1} - T_i}, \quad (\text{D1})$$

and then integrating it across fields as in Eq. (7). The magnetization data $M(H)$ were linearly interpolated along the field direction in steps of 0.1 T before extraction of the magnetic entropy.

APPENDIX E: MAGNETOCALORIC PERFORMANCE PER MASS AND VOLUME

The measured magnetocaloric effect, normalized by volume and by mass, at $T = 2$ K for a field change from 9 to 0 T for $\text{Gd}_3\text{Mg}_2\text{Sb}_3\text{O}_{14}$ (kagome), $\text{Gd}_2\text{Sn}_2\text{O}_7$ (pyrochlore), and $\text{Gd}_3\text{Ga}_5\text{O}_{12}$ (garnet) and for a field change from 7 to 0 T for $\text{Ba}_2\text{GdSbO}_6$ (fcc), can be found in Table IV.

APPENDIX F: STRUCTURAL REFINEMENTS OF Gd COMPOUNDS

Rietveld analysis of the XRD data shows that the refined structures are consistent with the structures reported in the literature [24,25,27,29,30]. The Rietveld refinement of $\text{Gd}_3\text{Mg}_2\text{Sb}_3\text{O}_{15}$ and the corresponding refined crystal structure are shown in Figs. 11 and 12, respectively. Refinements for $\text{Ba}_2\text{GdSbO}_6$, $\text{Gd}_2\text{Sn}_2\text{O}_7$, and $\text{Gd}_3\text{Ga}_5\text{O}_{12}$

are shown in Figs. 13–15, respectively. Recently, the family of kagome compounds of the form Ln₃Mg₂Sb₃O₁₄ was found to exhibit sample-dependent cation site disorder, in which the Ln³⁺ ion on the 9d Wyckoff site of a kagome layer swaps places with a Mg²⁺ ion on the interlayer 3a site (see Fig. 12) [54,55]. We find a 10.5(2)% cation site disordering in the Gd₃Mg₂Sb₃O₁₄ sample in this work. A comparable amount of site disorder has been found in other samples of Ln₃Mg₂Sb₃O₁₄, including the emergent-charge-ordered kagome Ising magnet Dy₃Mg₂Sb₃O₁₄ [54] and the dipolar kagome ice Ho₃Mg₂Sb₃O₁₄ [55].

-
- [1] X. Moya and N. D. Mathur, Caloric materials for cooling and heating, *Science* **370**, 797 (2020).
 - [2] W. F. Giauque and D. P. MacDougall, Attainment of temperatures below 1° absolute by demagnetization of Gd₂(SO₄)₃·8H₂O, *Phys. Rev.* **43**, 768 (1933).
 - [3] P. Wikus, E. Canavan, S. T. Heine, K. Matsumoto, and T. Numazawa, Magnetocaloric materials and the optimization of cooling power density, *Cryogenics* **62**, 150 (2014).
 - [4] M. E. Zhitomirsky, Enhanced magnetocaloric effect in frustrated magnets, *Phys. Rev. B* **67**, 104421 (2003).
 - [5] Y.-C. Chen, J. Prokleska, W.-J. Xu, J.-L. Liu, J. Liu, W.-X. Zhang, J.-H. Jia, V. Sechovský, and M.-L. Tong, A brilliant cryogenic magnetic coolant: magnetic and magnetocaloric study of ferromagnetically coupled GdF₃, *J. Mater. Chem. C* **3**, 12206 (2015).
 - [6] D. A. P. Brasiliano, PhD thesis, Université Grenoble Alpes, 2017.
 - [7] Gd(OH)F₂: A promising cryogenic magnetic refrigerant, *J. Am. Chem. Soc.* **144**, 13787 (2022).
 - [8] G. Lorusso, J. Sharples, E. Palacios, O. Roubeau, E. Brechin, R. Sessoli, A. Rossin, F. Tuna, E. McInnes, D. Collison, and M. Evangelisti, A dense metal–organic framework for enhanced magnetic refrigeration, *Adv. Mater.* **25**, 4653 (2013).
 - [9] E. Palacios, J. A. Rodríguez-Velamazán, M. Evangelisti, G. J. McIntyre, G. Lorusso, D. Visser, L. J. de Jongh, and L. A. Boatner, Magnetic structure and magnetocalorics of GdPO₄, *Phys. Rev. B* **90**, 214423 (2014).
 - [10] M. S. Reis, Magnetocaloric and barocaloric effects of metal complexes for solid state cooling: Review, trends and perspectives, *Coord. Chem. Rev.* **417**, 213357 (2020).
 - [11] P. Mukherjee, Ph.D. thesis, University of Cambridge, Cambridge, Cambridgeshire, UK, 2018, publisher: Apollo - University of Cambridge Repository.
 - [12] D. A. Paixao Brasiliano, J.-M. Duval, C. Marin, E. Bichaud, J.-P. Brison, M. Zhitomirsky, and N. Luchier, YbGG material for adiabatic demagnetization in the 100 mK–3 K range, *Cryogenics* **105**, 103002 (2020).
 - [13] Z. L. Dun, J. Trinh, K. Li, M. Lee, K. W. Chen, R. Baumbach, Y. F. Hu, Y. X. Wang, E. S. Choi, B. S. Shastry, A. P. Ramirez, and H. D. Zhou, Magnetic Ground States of the Rare-Earth Tripod Kagome Lattice Mg₂RESB₃O₁₄ (RE = Gd, Dy, Er), *Phys. Rev. Lett.* **116**, 157201 (2016).
 - [14] O. A. Petrenko and D. McK. Paul, Classical Heisenberg antiferromagnet on a garnet lattice: A Monte Carlo simulation, *Phys. Rev. B* **63**, 024409 (2000).
 - [15] E. C. Koskelo, C. Liu, P. Mukherjee, N. D. Kelly, and S. E. Dutton, Free-spin dominated magnetocaloric effect in dense Gd³⁺ double perovskites, *Chem. Mater.* **34**, 3440 (2022).
 - [16] The soft modes are quartic modes, whose energy is given by $Ax_k^4 + Cx_k^2y_k^2 + By_k^4$.
 - [17] N. d’Ambrumenil, O. A. Petrenko, H. Mutka, and P. P. Deen, Dispersionless Spin Waves and Underlying Field-Induced Magnetic Order in Gadolinium Gallium Garnet, *Phys. Rev. Lett.* **114**, 227203 (2015).
 - [18] G. Jackeli and M. E. Zhitomirsky, Frustrated Antiferromagnets at High Fields: Bose-Einstein Condensation in Degenerate Spectra, *Phys. Rev. Lett.* **93**, 017201 (2004).
 - [19] M. E. Zhitomirsky, Real-space perturbation theory for frustrated magnets: application to magnetization plateaus, *J. Phys.: Conf. Series* **592**, 012110 (2015).
 - [20] N_2 are harmonic modes, whose energy in terms of generalized coordinates x_k and y_k is expanded as $Ax_k^2 + By_k^2$.
 - [21] S. S. Sosin, L. A. Prozorova, A. I. Smirnov, A. I. Golov, I. B. Berkutov, O. A. Petrenko, G. Balakrishnan, and M. E. Zhitomirsky, Magnetocaloric effect in pyrochlore antiferromagnet Gd₂Ti₂O₇, *Phys. Rev. B* **71**, 094413 (2005).
 - [22] M. E. Zhitomirsky and H. Tsunetsugu, High field properties of geometrically frustrated magnets, *Prog. Theor. Phys. Suppl.* **160**, 361 (2005).
 - [23] R. Schick, T. Ziman, and M. E. Zhitomirsky, Quantum versus thermal fluctuations in the fcc antiferromagnet: Alternative routes to order by disorder, *Phys. Rev. B* **102**, 220405 (2020).
 - [24] Z. L. Dun, J. Trinh, M. Lee, E. S. Choi, K. Li, Y. F. Hu, Y. X. Wang, N. Blanc, A. P. Ramirez, and H. D. Zhou, Structural and magnetic properties of two branches of the tripod-kagome-lattice family A₂R₃Sb₃O₁₄ (A = Mg, Zn; R = Pr, Nd, Gd, Tb, Dy, Ho, Er, Yb), *Phys. Rev. B* **95**, 104439 (2017).
 - [25] C. Wellm, J. Zeisner, A. Alfonsov, M.-I. Sturza, G. Bastien, S. Gaß, S. Wurmehl, A. U. B. Wolter, B. Büchner, and V. Kataev, Magnetic interactions in the tripod kagome antiferromagnet Mg₂Gd₃Sb₃O₁₄ probed by static magnetometry and high-field ESR spectroscopy, *Phys. Rev. B* **102**, 214414 (2020).
 - [26] V. Bondah-Jagalu and S. T. Bramwell, Magnetic susceptibility study of the heavy rare-earth stannate pyrochlores, *Can. J. Phys.* **79**, 1381 (2001).
 - [27] A. C. S. Hamilton, G. I. Lampronti, S. E. Rowley, and S. E. Dutton, Enhancement of the magnetocaloric effect driven by changes in the crystal structure of Al-doped GGG, Gd₃Ga_{5-x}Al_xO₁₂ (0 ≤ x ≤ 5), *J. Phys.: Condens. Matter* **26**, 116001 (2014).
 - [28] B. Melot, J. Drewes, R. Seshadri, E. Stoudenmire, and A. Ramirez, Magnetic phase evolution in the spinel compounds Zn_{1-x}Co_xCr₂O₄, *J. Phys.: Condens. Matter* **21**, 216007 (2009).
 - [29] H. Karunadasa, Q. Huang, B. G. Ueland, P. Schiffer, and R. J. Cava, Ba₂LnSbO₆ and Sr₂LnSbO₆ (Ln = Dy, Ho, Gd) double perovskites: Lanthanides in the geometrically frustrating fcc lattice, *Proc. Natl. Acad. Sci.* **100**, 8097 (2003).

- [30] J. Paddison, G. Ehlers, O. Petrenko, A. Wildes, J. Gardner, and J. Stewart, Spin correlations in the dipolar pyrochlore antiferromagnet $\text{Gd}_2\text{Sn}_2\text{O}_7$, *J. Phys.: Condens. Matter* **29**, 144001 (2017).
- [31] J. Paddison, H. Jacobsen, O. Petrenko, M. Fernández-Díaz, P. Deen, and A. Goodwin, Hidden order in spin-liquid $\text{Gd}_3\text{Ga}_5\text{O}_{12}$, *Science* **350**, 179 (2015).
- [32] The progressive discrepancy observed between experiments and Monte Carlo simulations at large applied fields is likely due to spin quantization effects.
- [33] We notice a discrepancy between Monte Carlo simulations and experiments at small field values and low temperatures in the kagome case, the origin of which remains unclear.
- [34] P. Mukherjee, Y. Wu, G. I. Lampronti, and S. E. Dutton, Magnetic properties of monoclinic lanthanide orthoborates, LnBO_3 , $\text{Ln}=\text{Gd}, \text{Tb}, \text{Dy}, \text{Ho}, \text{Er}, \text{Yb}$, *Mater. Res. Bull.* **98**, 173 (2018).
- [35] M. Ashtar, Y. Bai, L. Xu, Z. Wan, Z. Wei, Y. Liu, M. Marwat, and Z. Tian, Structure and magnetic properties of melilite-type compounds $\text{RE}_2\text{Be}_2\text{GeO}_7$ ($\text{RE} = \text{Pr}, \text{Nd}, \text{Gd-Yb}$) with rare-earth ions on Shastry–Sutherland lattice, *Inorg. Chem.* **60**, 3626 (2021).
- [36] Y.-C. Chen, L. Qin, Z.-S. Meng, D.-F. Yang, C. Wu, Z. Fu, Y.-Z. Zheng, J.-L. Liu, R. Tarasenko, M. Orendáč, J. Prokleška, V. Sechovský, and M.-L. Tong, Study of a magnetic-cooling material $\text{Gd}(\text{OH})\text{CO}_3$, *J. Mater. Chem. A* **2**, 9851 (2014).
- [37] N. D. Kelly and S. E. Dutton, Magnetic properties of quasi-one-dimensional lanthanide calcium oxyborates $\text{Ca}_4\text{LnO}(\text{BO}_3)_3$, *Inorg. Chem.* **59**, 9188 (2020), pMID: 32525304.
- [38] P. J. Saines and N. C. Bristow, Probing magnetic interactions in metal–organic frameworks and coordination polymers microscopically, *Dalton Trans.* **47**, 13257 (2018).
- [39] J. Hellsvik, R. D. Pérez, R. M. Geihufe, M. Måansson, and A. V. Balatsky, Spin wave excitations of magnetic metal–organic materials, *Phys. Rev. Mater.* **4**, 024409 (2020).
- [40] J. D. Bocarsly, E. E. Levin, S. A. Humphrey, T. Faske, W. Donner, S. D. Wilson, and R. Seshadri, Magnetostructural coupling drives magnetocaloric behavior: The case of MnB versus FeB, *Chem. Mater.* **31**, 4873 (2019).
- [41] H. Karunadasa, Q. Huang, B. G. Ueland, J. W. Lynn, P. Schiffer, K. A. Regan, and R. J. Cava, Honeycombs of triangles and magnetic frustration in Sr_LO_4 ($L = \text{Gd}, \text{Dy}, \text{Ho}, \text{Er}, \text{Tm}, \text{and Yb}$), *Phys. Rev. B* **71**, 144414 (2005).
- [42] T. Numazawa, K. Kamiya, T. Okano, and K. Matsumoto, Magnetocaloric effect in $(\text{Dy}_x\text{Gd}_{1-x})_3\text{Ga}_5\text{O}_{12}$ for adiabatic demagnetization refrigeration, *Phys. B: Condens. Matter* **329–333**, 1656 (2003).
- [43] P. Mukherjee, A. C. S. Hamilton, H. F. J. Glass, and S. E. Dutton, Sensitivity of magnetic properties to chemical pressure in lanthanide garnets $\text{Ln}_3\text{A}_2\text{X}_3\text{O}_{12}$, $\text{Ln} = \text{Gd}, \text{Tb}, \text{Dy}$, Ho, A = Ga, Sc, In, Te, X = Ga, Al, Li, *J. Phys.: Condens. Matter* **29**, 405808 (2017).
- [44] M. Orendáč, J. Hanko, E. Čižmár, A. Orendáčová, M. Shirai, and S. T. Bramwell, Magnetocaloric study of spin relaxation in dipolar spin ice $\text{Dy}_2\text{Ti}_2\text{O}_7$, *Phys. Rev. B* **75**, 104425 (2007).
- [45] S. Sosin, L. Prozorova, A. Smirnov, A. Golov, I. Berkutov, O. Petrenko, G. Balakrishnan, and M. Zhitomirsky, Adiabatic demagnetization of a pyrochlore antiferromagnet $\text{Gd}_2\text{Ti}_2\text{O}_7$, *J. Magn. Magn. Mater.* **290–291**, 709 (2005), proceedings of the Joint European Magnetic Symposia (JEMS' 04).
- [46] E. C. Koskelo, N. D. Kelly, L. A. V. Nagle-Cocco, J. D. Bocarsly, P. Mukherjee, C. Liu, Q. Zhang, and S. E. Dutton, Magnetic and magnetocaloric properties of the $\text{A}_2\text{Ln SbO}_6$ lanthanide oxides on the frustrated *fcc* lattice, *Inorg. Chem.* **62**, 10317 (2023).
- [47] M. B. Sanders, K. M. Baroudi, J. W. Krizan, O. A. Mukadam, and R. J. Cava, Synthesis, crystal structure, and magnetic properties of novel 2D kagome materials $\text{RE}_3\text{Sb}_3\text{Mg}_2\text{O}_{14}$ ($\text{RE} = \text{La}, \text{Pr}, \text{Sm}, \text{Eu}, \text{Tb}, \text{Ho}$): Comparison to $\text{RE}_3\text{Sb}_3\text{Zn}_2\text{O}_{14}$ family, *Physica Status Solidi (B)* **253**, 2056 (2016).
- [48] M. B. Sanders, J. W. Krizan, and R. J. Cava, $\text{RE}_3\text{Sb}_3\text{Zn}_2\text{O}_{14}$ ($\text{RE} = \text{La}, \text{Pr}, \text{Nd}, \text{Sm}, \text{Eu}, \text{Gd}$): a new family of pyrochlore derivatives with rare earth ions on a 2D kagome lattice, *J. Mater. Chem. C* **4**, 541 (2016).
- [49] <https://doi.org/10.17863/CAM.99920>.
- [50] L. B. McCusker, R. B. Von Dreele, D. E. Cox, D. Louë, and P. Scardi, Rietveld refinement guidelines, *J. Appl. Crystallogr.* **32**, 36 (1999).
- [51] A. Coelho, *TOPAS* and *TOPAS-Academic*: an optimization program integrating computer algebra and crystallographic objects written in C++, *J. Appl. Crystallogr.* **51**, 210 (2018).
- [52] P. Thompson, D. E. Cox, and J. B. Hastings, Rietveld refinement of Debye–Scherrer synchrotron X-ray data from Al_2O_3 , *J. Appl. Crystallogr.* **20**, 79 (1987).
- [53] B. J. Kennedy, B. A. Hunter, and C. J. Howard, Structural and bonding trends in tin pyrochlore oxides, *J. Solid State Chem.* **130**, 58 (1997).
- [54] J. M. Paddison, H. Ong, J. Hamp, P. Mukherjee, X. Bai, M. Tucker, N. Butch, C. Castelnovo, M. Mourigal, and S. Dutton, Emergent order in the kagome Ising magnet $\text{Dy}_3\text{Mg}_2\text{Sb}_3\text{O}_{14}$, *Nat. Commun.* **7**, 13842 (2016).
- [55] Z. Dun, X. Bai, J. A. M. Paddison, E. Hollingworth, N. P. Butch, C. D. Cruz, M. B. Stone, T. Hong, F. Demmel, M. Mourigal, and H. Zhou, Quantum versus Classical Spin Dragmentation in Dipolar Kagome Ice $\text{Ho}_3\text{Mg}_2\text{Sb}_3\text{O}_{14}$, *Phys. Rev. X* **10**, 031069 (2020).
- [56] K. Momma and F. Izumi, *VESTA 3* for three-dimensional visualization of crystal, volumetric and morphology data, *J. Appl. Crystallogr.* **44**, 1272 (2011).